Numerical Solution of Anisotropic Biot Equations in Quasi-static State

Sergey Solovyev[1], Mikhail Novikov[2(✉)], and Vadim Lisitsa[1]

[1] Institute of Mathematics SB RAS, Koptug ave. 4, Novosibirsk 630090, Russia
lisitsavv@ipgg.sbras.ru
[2] Institute of Petroleum Geology and Geophysics SB RAS, Koptug ave. 3, Novosibirsk 630090, Russia
novikovma@ipgg.sbras.ru

Abstract. Frequency-dependent seismic attenuation can be applied to indicate transport properties of fractured media and fluid mobility within it. In particular, wave-induced fluid flow (WIFF) appears during seismic wave propagation between fractures and background as well as within interconnected fractures, and causes intensive attenuation. We present effective algorithm for numerical upscaling to estimate attenuation in anisotropic fractured porous fluid-saturated media. Algorithm is based on numerical solution of quasi-static Biot equations using finite-difference approximation. Presented algorithm is used to estimate seismic attenuation in fractured media with high fracture connectivity. Results of numerical experiments demonstrate the influence of physical properties and microscale anisotropy of fracture-filling material on seismic attenuation.

Keywords: Poroelaticity · Wave-induced fluid flow · Quasi-static state · Finite differences · Direct methods for SLAE

1 Introduction

Modern challenges in geophysics for seismic monitoring methods (4D seismic) are motivated by the developing of such fields as CO_2 sequestration [8,13] and geothermal energy exploration [11,18]. In particular, transport properties of fractured reservoir, fluid mobility should be estimated properly using obtained seismic data. One popular seismic attribute in modern research is seismic attenuation. In fluid-saturated media seismic wave generates fluid pressure gradients on the interfaces and induces fluid flows, significantly affected by mesoscale geometry structure of reservoir as well as microscale properties of rock (porosity, permeability etc.) and fluid properties. Low-frequency wave (having large wave cycle)

S.S. developed the algorithm and V.L. designed the experiments under the support of RSCF grant no. 19-77-20004. M.N. performed the analysis of the results. Numerical simulations were performed using the supercomputer facilities of Siberian Supercomputer Center (Cluster NKS-30T).

© The Author(s), under exclusive license to Springer Nature Switzerland AG 2022
O. Gervasi et al. (Eds.): ICCSA 2022 Workshops, LNCS 13378, pp. 310–327, 2022.
https://doi.org/10.1007/978-3-031-10562-3_23

propagation provide enough time for fracture-to-background flow (FB-WIFF) to form. FB-WIFF is most intensive at low frequencies and depends mostly on the contrast of physical properties between background rock and fracture-filling material [10,16]. Intensive wave-induced fluid flow also appear during high frequency wave propagation between intersecting fractures (fracture-to-fracture WIFF, FF-WIFF). This flow is defined by fracture-filling material properties and fracture connectivity [7,10,16]. Theoretical study of FF-WIFF effect consider relatively simple fractured media structure, and fracture connectivity is presented by intersecting pairs of differently oriented fractures [10]. FF-WIFF phenomena is also studied numerically, but recent studies are often restricted by the same fracture connectivity criteria [10,16]. One exception is study [9] where authors apply discrete fracture network of more complex structure and then stronger connectivity. Also, studies are mostly limited by isotropic case [9,19], when significant anisotropy of elastic and transport properties is typical for rocks, for example, affected by partial dissolution by CO_2. For finite-difference or finite-element approach to simulate seismic wave propagation or creeping test for fractured porous media grid step depends on fracture width, and computation domain size depends on representative volume [1,15] to consider typical percolation length and fracture connectivity [14,21]. Moreover, to obtain effective attenuation estimations numerical upscaling requires a series of experiments for statistically equivalent model of the fracture system. Thus, an efficient numerical upscaling algorithm should be able to solve series on large-scale problems including the microscale anisotropy of the media.

In this paper, we continue and extend our previous studies in numerical solution of quasi-static Biot equations [19] to anisotropic case and present an algorithm for numerical upscaling to estimate effective properties of fractured-porous anisotropic media in low-frequency range. To do so, we develop the algorithm to solve anisotropic Biot equations in quasi-static state. Finite-difference approximation of Biot anisotropic equations is applied to solve boundary value problem to calculate stress-strain behaviour in anisotropic fractured porous fluid-saturated sample. Set of stress-strain state problems form poroelastic media upscaling problem to obtain frequency-dependent stiffness tensor, corresponding to the visco-elastic media. We consider details of the numerical solution of the SLAE resulting from Biot equations approximation. We perform a set of numerical experiments using our algorithm demonstrating the effect of fracture-filling material properties and anisotropy on frequency-dependent attenuation caused by wave-induced fluid flow within highly connected fracture system.

2 Stress-Strain Behaviour in Poroelastic Fluid-Saturated Problem Set Up

2.1 Anisotropic Biot Equations in Quasi-static State

To calculate the stress-strain state in porous fluid-saturated media we consider the anisotropic quasi-static Biot equations in frequency domain governing the

diffusion processes in fluid-filled poroelastic anisotropic media in a low-frequency regimes [2,3]. In Cartesian coordinates and 2D case the equations can be written as follows:

$$\begin{aligned}
&\frac{\partial}{\partial x}\left[C_{11}(\omega)\frac{\partial u_x}{\partial x}+C_{13}(\omega)\frac{\partial u_z}{\partial z}+\alpha_1 M\left(\frac{\partial w_x}{\partial x}+\frac{\partial w_z}{\partial z}\right)\right]\\
&+\frac{\partial}{\partial z}\left[C_{55}(\omega)\left(\frac{\partial u_x}{\partial z}+\frac{\partial u_z}{\partial x}\right)\right]=0,\\
&\frac{\partial}{\partial x}\left[C_{55}(\omega)\left(\frac{\partial u_x}{\partial z}+\frac{\partial u_z}{\partial x}\right)\right]\\
&+\frac{\partial}{\partial z}\left[C_{13}(\omega)\frac{\partial u_x}{\partial x}+C_{33}(\omega)\frac{\partial u_z}{\partial z}+\alpha_2 M\left(\frac{\partial w_x}{\partial x}+\frac{\partial w_z}{\partial z}\right)\right]=0,\\
&\frac{\partial}{\partial x}\left[M\left(\alpha_1\frac{\partial u_x}{\partial x}+\alpha_2\frac{\partial u_z}{\partial z}\right)+M\left(\frac{\partial w_x}{\partial x}+\frac{\partial w_z}{\partial z}\right)\right]=i\omega\frac{\eta}{k_1}w_x,\\
&\frac{\partial}{\partial z}\left[M\left(\alpha_1\frac{\partial u_x}{\partial x}+\alpha_2\frac{\partial u_z}{\partial z}\right)+M\left(\frac{\partial w_x}{\partial x}+\frac{\partial w_z}{\partial z}\right)\right]=i\omega\frac{\eta}{k_2}w_z,
\end{aligned}\tag{1}$$

where $\boldsymbol{u}=(u_x,u_z)^T$ is the solid matrix displacement vector, $\boldsymbol{w}=(w_x,w_z)^T$ is the vector of the relative fluid displacement with respect to the solid matrix, C_{ij} is the frequency-dependent stiffness tensor C components of fluid-saturated material, α_1, α_2 are Biot-Willis parameters in axes directions, M is the fluid storage coefficient, η is the fluid dynamic viscosity, κ_1, κ_2 are the absolute permeability of the rock in axes directions, and ω is the temporal frequency. Parameters λ_u, M, and α_1, α_2 are defined by the drained material stiffness tensor and fluid and solid bulk moduli [6,12].

The strain tensor $\boldsymbol{\varepsilon}$ and its components are defined as

$$\boldsymbol{\varepsilon}=\begin{pmatrix}\varepsilon_{xx} & \varepsilon_{xz}\\ \varepsilon_{xz} & \varepsilon_{zz}\end{pmatrix}\quad \varepsilon_{xx}=\frac{\partial u_x}{\partial x},\quad \varepsilon_{zz}=\frac{\partial u_z}{\partial z},\quad \varepsilon_{xz}=\frac{1}{2}\left(\frac{\partial u_z}{\partial x}+\frac{\partial u_x}{\partial z}\right).\tag{2}$$

The following boundary conditions provide an unique solution of system (1):

$$\begin{aligned}
&\sigma_{xx}=C_{11}(\omega)\frac{\partial v_x}{\partial x}+C_{13}(\omega)\frac{\partial v_z}{\partial z}\Big|_{x=L_1^x}=\phi_x\\
&\boldsymbol{w}\cdot\boldsymbol{n}|_{\partial D}=0.
\end{aligned}\tag{3}$$

Here the first condition is the normal compression at the boundary, and second one is the torsion of domain and the third – no-flow boundary condition at all boundaries.

2.2 Effective Viscoelastic Media

We aim to reconstruct the effective viscoelastic media, so that for any stresses σ_0 applied to a unit volume the average strains in the reconstructed anisotropic

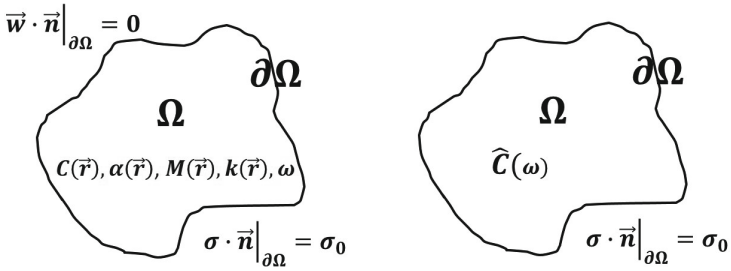

Fig. 1. Anisotropic media: original fluid-saturated poroelastic media (left); reconstructed effective frequency-dependent viscoelastic media (right). $C(\boldsymbol{r}), \alpha(\boldsymbol{r}), M(\boldsymbol{r})$, $k((\boldsymbol{r}))$ are the space dependent parameters of Eq. (1), $\boldsymbol{n}$ is the outer normal.

(Fig. 1, right) and the original fluid-saturated poroelastic media (Fig. 1, left) should coincide. By reconstruction we mean retrieving the frequency-dependent effective stiffness tensor $\hat{C}$, such that

$$\begin{aligned}
&\frac{\partial}{\partial x}\left[\hat{C}_{11}(\omega)\frac{\partial v_x}{\partial x}+\hat{C}_{13}(\omega)\frac{\partial v_z}{\partial z}\right]+\frac{\partial}{\partial z}\left[\hat{C}_{55}(\omega)(\frac{\partial v_x}{\partial z}+\frac{\partial v_z}{\partial x})\right]=0,\\
&\frac{\partial}{\partial x}\left[\hat{C}_{55}(\omega)(\frac{\partial v_x}{\partial z}+\frac{\partial v_z}{\partial x})\right]+\frac{\partial}{\partial z}\left[\hat{C}_{13}(\omega)\frac{\partial v_x}{\partial x}+\hat{C}_{33}(\omega)\frac{\partial v_z}{\partial z}\right]=0,
\end{aligned} \tag{4}$$

where $\boldsymbol{v}=(v_x,v_z)^2$ is the displacement vector in viscoelastic media.

Therefore, we need to compute reconstructed tensor $\hat{C}$ (which is constant in Ω) by the space-dependent parameters $C, \alpha_x, \alpha_z, M, k_1, k_2$ in the same geometry in terms of average strains $\int_\Omega \varepsilon dv = \int_\Omega \hat{\varepsilon} dv = I_\varepsilon$ ($\varepsilon \in \{\varepsilon_{xx}, \varepsilon_{zz}, \varepsilon_{xz}\}$) and same stress σ_0 at the boundary $\partial\Omega$. The strains ε distributions in original medium satisfy the solution of the Eq. (1) with boundary conditions (Fig. 1, left). Thus for $\sigma \in \{\sigma_{xx}, \sigma_{zz}, \sigma_{xz}\}$ (components of stress tensor in porous fluid-saturated media) $\int_\Omega \sigma dv = \int_\Omega \hat{\sigma} dv = I_\sigma$.

The strains ε distributions in original medium satisfy the solution of the Eqs. (1) with boundary conditions (Fig. 1, left).

In reconstructed medium $I_\sigma = \int_\Omega \hat{\sigma} dv = \int_\Omega \hat{C}\hat{\varepsilon} dv = \hat{C}\int_\Omega \hat{\varepsilon} dv = \hat{C} I_\varepsilon$

We obtain the SLAE $I_\sigma = \hat{C} I_\varepsilon$ with three equations and nine unknown tensor $\hat{C}$ components:

$$\begin{aligned}
I_{\sigma xx} &= \hat{C}_{11} I_{\varepsilon xx} + \hat{C}_{13} I_{\varepsilon zz} + \hat{C}_{15} I_{\varepsilon xz},\\
I_{\sigma zz} &= \hat{C}_{31} I_{\varepsilon xx} + \hat{C}_{33} I_{\varepsilon zz} + \hat{C}_{35} I_{\varepsilon xz},\\
I_{\sigma xz} &= \hat{C}_{51} I_{\varepsilon xx} + \hat{C}_{53} I_{\varepsilon zz} + \hat{C}_{55} I_{\varepsilon xz}.
\end{aligned} \tag{5}$$

As the solution for $\hat{C}$ is not unique, we need to perform at least three experiments with different sets of boundary conditions to determine the system (5). The strain tensors $I_\varepsilon^{(1)}, I_\varepsilon^{(2)}, I_\varepsilon^{(3)}$ and stress tensors $I_\sigma^{(1)}, I_\sigma^{(2)}, I_\sigma^{(3)}$ obtained as solutions of the system (1) with boundary conditions $\sigma_0^{(1)}$, $\sigma_0^{(2)}$ and $\sigma_0^{(3)}$, correspondingly, are used to construct SLAE with unique solution:

$$
\begin{aligned}
I^{(1)}_{\sigma xx} &= \hat{C}_{11} I^{(1)}_{\varepsilon xx} + \hat{C}_{13} I^{(1)}_{\varepsilon zz} + \hat{C}_{15} I^{(1)}_{\varepsilon xz},\\
I^{(1)}_{\sigma zz} &= \hat{C}_{31} I^{(1)}_{\varepsilon xx} + \hat{C}_{33} I^{(1)}_{\varepsilon zz} + \hat{C}_{35} I^{(1)}_{\varepsilon xz},\\
I^{(1)}_{\sigma xz} &= \hat{C}_{51} I^{(1)}_{\varepsilon xx} + \hat{C}_{53} I^{(1)}_{\varepsilon zz} + \hat{C}_{55} I^{(1)}_{\varepsilon xz},\\
I^{(2)}_{\sigma xx} &= \hat{C}_{11} I^{(2)}_{\varepsilon xx} + \hat{C}_{13} I^{(2)}_{\varepsilon zz} + \hat{C}_{15} I^{(2)}_{\varepsilon xz},\\
I^{(2)}_{\sigma zz} &= \hat{C}_{31} I^{(2)}_{\varepsilon xx} + \hat{C}_{33} I^{(2)}_{\varepsilon zz} + \hat{C}_{35} I^{(2)}_{\varepsilon xz},\\
I^{(2)}_{\sigma xz} &= \hat{C}_{51} I^{(2)}_{\varepsilon xx} + \hat{C}_{53} I^{(2)}_{\varepsilon zz} + \hat{C}_{55} I^{(2)}_{\varepsilon xz},\\
I^{(3)}_{\sigma xx} &= \hat{C}_{11} I^{(3)}_{\varepsilon xx} + \hat{C}_{13} I^{(3)}_{\varepsilon zz} + \hat{C}_{15} I^{(3)}_{\varepsilon xz},\\
I^{(3)}_{\sigma zz} &= \hat{C}_{31} I^{(3)}_{\varepsilon xx} + \hat{C}_{33} I^{(3)}_{\varepsilon zz} + \hat{C}_{35} I^{(3)}_{\varepsilon xz},\\
I^{(3)}_{\sigma xz} &= \hat{C}_{51} I^{(3)}_{\varepsilon xx} + \hat{C}_{53} I^{(3)}_{\varepsilon zz} + \hat{C}_{55} I^{(3)}_{\varepsilon xz},
\end{aligned}
\tag{6}
$$

2.3 Upscaling Procedure

To reconstruct the effective viscoelastic tensor we consider a rectangular domain $D = [L_1^x, L_2^x] \times [L_1^z, L_2^z]$ of anisotropic poroelastic fluid-saturated media with boundary condition $\sigma \cdot \boldsymbol{n} = \sigma_0 = (\sigma_{01}, \sigma_{02})^t$ in following form:

$$
\begin{aligned}
&(\sigma_{xx}, \sigma_{xz})^t|_x = L_1^x, x = L_2^x = (\sigma_{01}, \sigma_{02})^t = (\phi_x, \psi),\\
&(\sigma_{xz}, \sigma_{zz})^t|_z = L_1^z, z = L_2^z = (\sigma_{01}, \sigma_{02})^t = (\psi, \phi_z),
\end{aligned}
\tag{7}
$$

where ϕ_x is the load σ_{xx} at the left and right faces; ϕ_z is the load σ_{zz} at the down and top faces; ψ – the value of σ_{xz} at each face.

The boundary conditions for the solid matrix velocity vector $(u_x, u_z)^T$ and for the relative fluid velocity $(w_x, w_z)^T$ vector are set by applying the equations [6].

$$
\begin{aligned}
\sigma_{xx} &= C_{11} \tfrac{\partial u_x}{\partial x} + C_{13} \tfrac{\partial u_z}{\partial z} + \alpha_1 M \left(\tfrac{\partial w_x}{\partial x} + \tfrac{\partial w_z}{\partial z} \right)\\
\sigma_{zz} &= C_{13} \tfrac{\partial u_x}{\partial x} + C_{33} \tfrac{\partial u_z}{\partial z} + \alpha_2 M \left(\tfrac{\partial w_x}{\partial x} + \tfrac{\partial w_z}{\partial z} \right)\\
\sigma_{xz} &= C_{55} \left(\tfrac{\partial u_x}{\partial z} + \tfrac{\partial u_z}{\partial x} \right).
\end{aligned}
\tag{8}
$$

Note that in the corners of domain both conditions of (7) must be taken into account. Therefore the full set of boundary conditions for Eqs. (1) in terms of velocity are the following:

1. Left and right faces, normal load:

$$
\sigma_{xx} = C_{11} \frac{\partial u_x}{\partial x} + C_{13} \frac{\partial u_z}{\partial z} + \alpha_1 M \left(\frac{\partial w_x}{\partial x} + \frac{\partial w_z}{\partial z} \right) = \phi_x
$$

2. Down and top faces, normal load:

$$
\sigma_{zz} = C_{13} \frac{\partial u_x}{\partial x} + C_{33} \frac{\partial u_z}{\partial z} + \alpha_2 M \left(\frac{\partial w_x}{\partial x} + \frac{\partial w_z}{\partial z} \right) = \phi_z
$$

3. All faces, shear load:

$$\sigma_{xz} = C_{55}\left(\frac{\partial u_x}{\partial z} + \frac{\partial u_z}{\partial x}\right) = \psi$$

4. Corners of the left and right faces, normal load:

$$\sigma_{xx} - \frac{C_{13}}{C_{33}}\sigma_{zz} = \left(C_{11} - \frac{C_{13}^2}{C_{33}}\right)\frac{\partial u_x}{\partial x} + M\left(\alpha_1 - \alpha_2\frac{C_{13}}{C_{33}}\right)\frac{\partial w_x}{\partial x} + M\left(\alpha_1 - \alpha_2\frac{C_{13}}{C_{33}}\right)\frac{\partial w_z}{\partial z} = \phi_x - \frac{C_{13}}{C_{33}}\phi_z$$

5. Corners of the down and top faces, normal load:

$$\sigma_{zz} - \frac{C_{13}}{C_{11}}\sigma_{xx} = \left(C_{33} - \frac{C_{13}^2}{C_{11}}\right)\frac{\partial u_z}{\partial z} + M\left(\alpha_2 - \alpha_1\frac{C_{13}}{C_{11}}\right)\frac{\partial w_x}{\partial x} + M\left(\alpha_2 - \alpha_1\frac{C_{13}}{C_{11}}\right)\frac{\partial w_z}{\partial z} = \phi_z - \frac{C_{13}}{C_{11}}\phi_x$$

6. Left and right faces, no-flow condition:

$$w_x = 0$$

7. Down and top faces, no-flow condition:

$$w_z = 0$$

b Schematic picture of domain (Fig. 2) demonstrate the distribution of applied boundary conditions at domain boundaries.

In particular, we consider three sets of boundary conditions (7) with basic loads:

– x-direction uniaxial compression:

$$\phi_x = 1, \quad \phi_z = 0, \quad \psi = 0; \tag{9}$$

– z-direction uniaxial compression:

$$\phi_x = 0, \quad \phi_z = 1, \quad \psi = 0; \tag{10}$$

– xz-torsion:

$$\phi_x = 0, \quad \phi_z = 0, \quad \psi = 1; \tag{11}$$

Details of the numerical solution of Biot equations (1) with presented boundary conditions (Sect. 2.3) are described below.

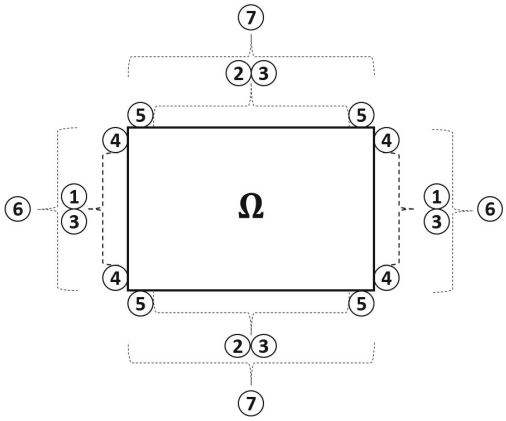

Fig. 2. Positions at the domain of the seven kinds boundary conditions.

3 Numerical Solution of Biot Equations

For numerical solution of Biot equations (1) we apply domain discretization by the rectangular grid $N_x \times N_z$. The domain boundaries cross the mesh at the centers of mesh edges as shown on Fig. 3.

Displacement x-components u_x and w_x are defined in the centers of vertical edges (z-edges), and z-components u_z and w_z are defined in the centers of horizontal edges (x-edges) (Fig. 4). The physical properties of the media $C_{11}, C_{13}, C_{33}, C_{55}, \alpha_1, \alpha_2, M$ are located in the middle nodes of the cells; η, k_1, k_2 – in the centers of the edges.

The first order partial derivatives $\frac{\partial}{\partial x}$ and $\frac{\partial}{\partial z}$ in Eq. (1) are approximated by the finite-differences. Solution components localization and derivatives discretization lead to the second order approximation of the first and the third equations of (1) in the centers of vertical edges, and the second and fourth equations in the centers of horizontal edges.

3.1 Approximation Stencils

The finite-difference approximation of Biot equations (1) leads to the four different stencils depending of the grid node. Each of them uses various number of unknowns (Fig. 5). Therefore, first and second equations of (1) use 16 components of total solution vector, third and fourth – 14 components. Boundary conditions (Sect. 2.3) approximation stencils are presented on the Fig. 6.

3.2 SLAE Construction

The Biot equations are approximated inside the computational domain (Fig. 3) and at its boundary. So $N_x \times N_z$ are performed $(N_x - 1)N_z$ approximations of the first and third equations and $N_x(N_z - 1)$ approximations of the second

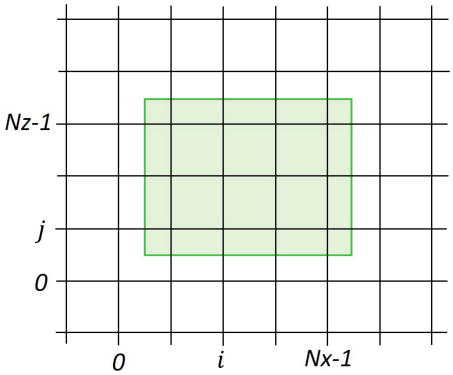

Fig. 3. Discretization of the computational domain.

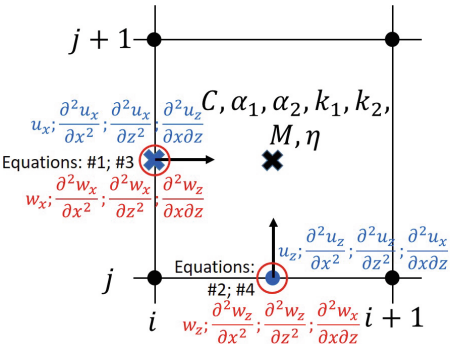

Fig. 4. Solution components, derivatives physical parameters location on computational grid, and nodes, where equations are approximated.

and fourth equations of (1) are performed on computational grid (approximated positions marked as "gray" circles at the Fig. 5). Total number of the linear equations is

$$N_{eq} = 2 * (N_x - 1)N_z + 2 * N_x(N_z - 1).$$

The stencils of such approximations cover the all internal points and points located out of the computational domain (see Fig. 7). So the number of unknown solution components in SLAE more than number of equations:

$$N_{un} = N_{eq} + 4 * N_x + 2 * (N_x - 1) + 4 * N_z + 2 * (N_z - 1).$$

Additional unknowns are excluded by boundary conditions. The external points are removed by boundary conditions (Sect. 2.3) with stencils (Fig. 6). Numbering of these points is demonstrated on the Fig. 7.

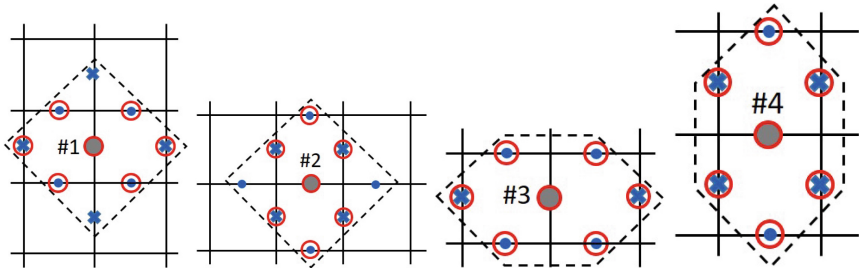

Fig. 5. Biot equations (1) stencils. Blue dots and crosses are solid matrix displacement components, red circles – fluid displacement components. (Color figure online)

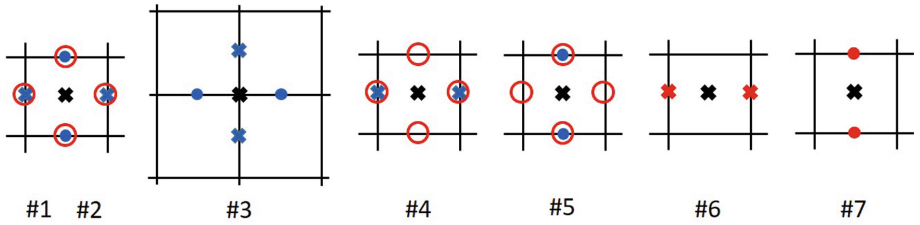

Fig. 6. Boundary condition stencils. Blue dots and crosses are solid matrix displacement components, red circles – fluid displacement components. (Color figure online)

By described approximation of equations and boundary conditions we obtain the consistent SLAE

$$\begin{gathered} Ax = b, \quad A \in \mathbb{C}^{N \times N}, \quad b \in \mathbb{C}^N, \\ N = N_{un} = N_{eq} = 2 * (N_x - 1)N_z + 2 * N_x(N_z - 1). \end{gathered} \tag{12}$$

3.3 Numerical SLAE Solution

The SLAE (12) is non-symmetrical with complex values, so the approach to solve it is the special topic which is out of scope of this paper. Moreover, the SLAE is ill-conditioned because of 2nd order boundary conditions.

To resolve this SLAE the robust commercial product Intel MKL PARDISO solver is used. It is based on direct methods and has appropriate efficiency and memory consumption to solve 2D problems.

First the optimal computational parameters were found to run the set of numerical experiments to reconstruct the effective viscoelastic media. The choice of major parameters (grid size and the number of frequencies) is done corresponding to used hardware (Intel(R) Xeon(R) CPU E5-2690 v2 @ 3.00 GHz with 10 cores and 256G RAM). In these performance experiments we used a grid with 1000 nodes in both spatial directions. The Biot equation is resolved for the set of 48 frequencies from 0 to $6.4 * 10^9$ Hz. The SLAE for each frequency is resolved for 3 different right hand sides raised from boundary conditions (9)–(11).

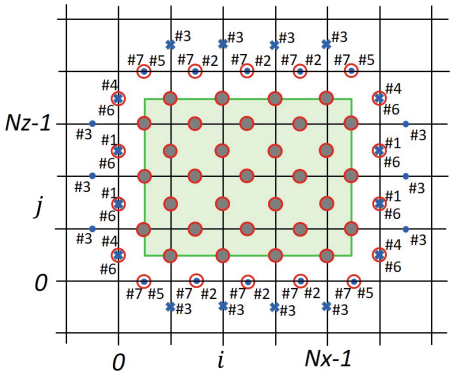

Fig. 7. Nodes, where Biot equations are approximated (gray circles) and unknowns are defined (gray, red circles, blue points and crosses). Numbering correspond to boundary conditions numerations. (Color figure online)

A single launch of the algorithm (one model, one frequency) include the following steps:

1. Approximate problem to get matrix A and right the hand sides b;
2. PARDISO Reordering step. It's a preliminary step to decrease memory consumption and time of the next factorization step;
3. PARDISO Factorization step. It perform LU decomposition of matrix A;
4. PARDISO Solve step. Solve the system to get solution x;
5. Postprocessing: Construct the stiffness tensor C.

Note that if the frequency is changed then only the main diagonal of the matrix A should be corrected. Thus, step (1) can be done for zero-frequency, but only diagonal entries are changed at further loops of the algorithm. The reordering step (2) depends only on position non-zero elements A, and can be done only once and applied for all ω. As a result, the entire algorithm (steps 1–5) is applied only to the first frequency in the raw, whereas the reduced version of the algorithm (steps 3–5) can be applied to all other frequencies.

The computational time for one model and all 48 frequencies is ≈3250 s. The timing profiling of the 48 runs is:

1. Approximate problem: ≈13 s.
2. PARDISO Reordering step: ≈20 s.
3. PARDISO Factorization step. 48× (≈57 s.)
4. PARDISO Solve step. 48× (≈7 s.)
5. Postprocessing: 48× (≈3 s.)

Execution of the algorithm for the problem size of 1000^2 requires about 18Gb RAM, thus it can be done on any desktop machine, or ported to a standard GP-GPU to improve performance.

4 Numerical Reconstruction of Effective Viscoelastic Media

To reconstruct effective viscoelastic stiffness tensor $\hat{C}$ we numerically compute the strain ($\boldsymbol{\varepsilon}(i,j)$) and the stress tensor components ($\boldsymbol{\sigma}(i,j)$) in the centers of the each cell:

$$\begin{aligned}
\varepsilon_{xx}(i,j) &= \frac{u_x(i+1,j) - u_x(i,j)}{h_x} \\
\varepsilon_{zz}(i,j) &= \frac{u_z(i,j+1) - u_z(i,j)}{h_z} \\
\varepsilon_{xz}(i,j) &= \frac{1}{2}\left(\frac{u_x(i,j) - u_x(i-1,j)}{h_z} + \frac{u_z(i,j) - u_z(i,j-1)}{h_z}\right) \\
Dw(i,j) &= \frac{w_x(i+1,j) - w_x(i,j)}{h_x} + \frac{w_z(i,j+1) - w_z(i,j)}{h_z} \\
\sigma_{xx}(i,j) &= C_{11}(i,j)\varepsilon_{xx}(i,j) + C_{13}(i,j)\varepsilon_{xx}(i,j) + \alpha_1(i,j)M(i,j)Dw(i,j) \\
\sigma_{zz}(i,j) &= C_{13}(i,j)\varepsilon_{xx}(i,j) + C_{33}(i,j)\varepsilon_{zz}(i,j) + \alpha_2(i,j)M(i,j)Dw(i,j) \\
\sigma_{xz}(i,j) &= C_{55}(i,j)\varepsilon_{xz}(i,j)
\end{aligned} \tag{13}$$

$$\begin{aligned}
I_{\varepsilon xx} &= \sum_{\Omega} \varepsilon_{xx}(i,j) \;\; I_{\sigma xx} = \sum_{\Omega} \sigma_{xx}(i,j) \\
I_{\varepsilon zz} &= \sum_{\Omega} \varepsilon_{zz}(i,j) \;\; I_{\sigma zz} = \sum_{\Omega} \sigma_{zz}(i,j) \\
I_{\varepsilon xz} &= \sum_{\Omega} \varepsilon_{xz}(i,j) \;\; I_{\sigma xz} = \sum_{\Omega} \sigma_{xz}(i,j)
\end{aligned} \tag{14}$$

To reconstruct the tensor $\hat{C}$, the SLAE 9×9 (6), with coefficients (14) should be solved.

It is convenient to apply seismic characteristics comparison except of effective stiffness tensor itself. So in all the numerical experiments we follow [4,20] to estimate the velocities and quality factors from complex frequency-dependent stiffness tensor components:

$$\begin{aligned}
V_{px} &= \Re\sqrt{\frac{\hat{C}_{11}}{\rho}}, \; V_{pz} = \Re\sqrt{\frac{\hat{C}_{33}}{\rho}}, \; V_s = \Re\sqrt{\frac{\hat{C}_{55}}{\rho}}, \\
Q_{px} &= \frac{\Re\hat{C}_{11}}{\Im\hat{C}_{11}}, \quad Q_{pz} = \frac{\Re\hat{C}_{33}}{\Im\hat{C}_{33}}, \quad Q_s = \frac{\Re\hat{C}_{55}}{\Im\hat{C}_{55}}.
\end{aligned} \tag{15}$$

5 Numerical Experiments

We perform sets of numerical experiments to check quality of our approach of recovering effective viscoelastic anisotropic media in three aspects:

1. Approximation quality of the differential statement of Biot equation and boundary conditions. In particular, we apply comparison with analytic

velocity and attenuation (inverse quality factor $1/Q$) estimations for isotropic layered model. Such experiments help to estimate the quality of approximation for various number of layers and mesh points per one layer.
2. Quality of solving SLAE (12).
The SLAE is solved via external package Intel MKL PARDISO, and we control the relative residual (usually about 10^{-11}) for each right hand side.
3. Correctness of the formulation of the problem by stress-strain state computation for anisotropic poroelastic fractured fluid-saturated media and reconstruction of the effective viscoelastic media properties, resulting in velocity and attenuation estimation. Analysis of obtained results is provided.

5.1 Approximation Quality

Realistic material properties of isotropic layered model (see Table 1.) are taken from the paper [17].

Mesh Refinement on Fixed Geometry. The geometry of model is square wits size 0.8×0.8 m with 8 layers: four internal Material #2 layers, three internal Material #1 layers and one external half-covered at the top and down of model (see Fig. 8). To check the approximation quality we decrease the mesh step in both (x) and (z) directions: $hx = hz = 0.05,\ 0.05/2,\ 0.05/4,\ 0.05/8,\ 0.05/16,\ 0.05/32$ (Fig. 8). Therefore, the number of points per layer are 2, 4, 8, 16, 32, 64.

The results (Fig. 9) show the convergence of presented approximation scheme by the convergence of frequency-dependent estimations of inverse quality factor.

Extending the Layered Model Along Layers. Other experiments involve the stretching of the layered model along the layers. The "square", "rectangle" and "thin" geometry is considered (see Fig. 10). The number of layers is 32, the number of points per layer is 16. Three corresponding grids have sizes 512×512, 1024×512 and 2048×512.

Figure 11 shows the quality factor $\frac{1}{Q}$ and P-wave phase velocity V_p (normal to layers) estimations compared with analytical estimations [5]. The peak position of attenuation estimation is at the same frequency, and the values of $\frac{1}{Q}$ and P-wave V_p are well agreed in general. The attenuation along layers is decreased to zero (Fig. 12) with model stretching as expected. Figure 13 demonstrates P-wave and S-wave velocity dependence on incidence angle. Estimations behaviour is similar to results demonstrated in [17].

Table 1. Material properties of isotropic layered model.

	Material #1	Material #2
Grain bulk modulus, K_s (GPa)	37	37
Grain density, ρ_s (g/cc)	2.65	2.65
Porosity, ϕ	0.1	0.37
Dry rock bulk modulus, K_m (GPa)	26	2.68
Dry rock shear modulus, μ_m (GPa)	31	0.857
Permeability, k (D)	10^{-3}	1
Brine: Builk modulus, K_f (GPa)	2.25	2.25
Brine: Density, ρ_f (g/cc)	1.09	1.09
Brine: Viscosity,η(P)	0.01	0.01
Biot-Willis parameter α	0.297297297	0.927567567
$\frac{Fluid\ dynamic\ viscosity}{Absolute\ permeability\ of\ the\ rock}$, $\frac{\eta}{k_0}$	$1 * 10^{12}$	$1 * 10^{9}$
Fluid storage coefficient M	$20.0896787868906 * 10^{9}$	$5.57060118727366 * 10^{9}$

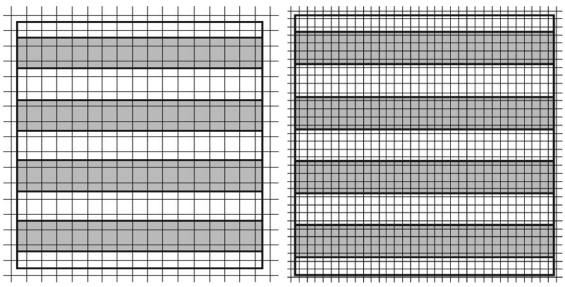

Fig. 8. Layered model geometry and mesh refinement. White layers have material #1 properties, black ones with material #2 properties from the Table 1.

5.2 Attenuation Estimation of Seismic Attenuation in Media with High Fracture Connectivity

We provide an example of described algorithm application to attenuation estimation in fractured porous fluid-saturated media. To study the influence of fracture-filling material physical properties and its anisotropy on seismic attenuation due to wave-induced fluid flow, we perform three sets of numerical experiments. We consider 8 realisations of fractured media model (example is shown on Fig. 14), containing two sets of vertical and horizontal fractures. Fractures are highly connected and form percolating chains through all domain. Details of corresponding fracture networks generation are described in [14]. Physical properties of isotropic background material are the same for all numerical experiments (Table 2, second column). We consider three fracture-filling materials, two isotropic – "stiff" (Table 2, third column) and "soft" (Table 2, fourth column), and one anisotropic, having different properties in horizontal and vertical fractures (Table 2, fifth and sixth columns, correspondingly).

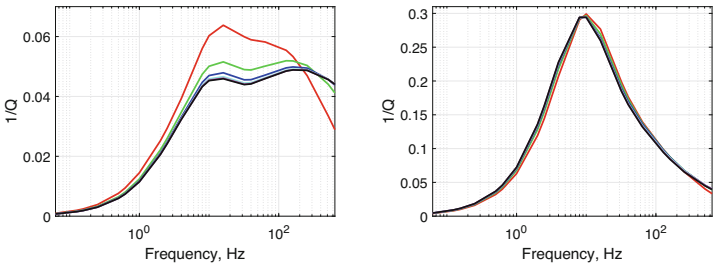

Fig. 9. Attenuation along layers (left) and normal to layers (right) for different grid step. Colors correspond to grid step decrease in the following order: red, green, blue, cyan, magenta, black. (Color figure online)

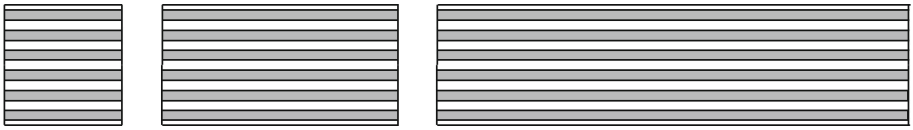

Fig. 10. The "square", "rectangle" and "thin" geometry.

Table 2. Physical properties of fractured media: background material (second column), isotropic fracture-filling materials (third and fourth columns), and anisotropic fracture-filling material for vertical and horizontal fractures (fifth and sixth columns).

	Background	"Stiff" fractures	"Soft" fractures	Horizontal frac	Vertical frac
C_{11}	$6.910 * 10^{10}$	$4.643 * 10^{10}$	$3.896 * 10^{10}$	$3.896 * 10^{10}$	$4.643 * 10^{10}$
C_{13}	$7.159 * 10^{10}$	$2.381 * 10^{10}$	$1.634 * 10^{10}$	$1.981 * 10^{10}$	$1.981 * 10^{10}$
C_{33}	$6.910 * 10^{10}$	$4.643 * 10^{10}$	$3.896 * 10^{10}$	$4.643 * 10^{10}$	$3.896 * 10^{10}$
C_{55}	$3.097 * 10^{10}$	$1.131 * 10^{10}$	$1.131 * 10^{10}$	$1.131 * 10^{10}$	$1.131 * 10^{10}$
M	$2.010 * 10^{10}$	$9.488 * 10^{9}$	$9.330 * 10^{9}$	$9.429 * 10^{9}$	$9.429 * 10^{9}$
$\alpha_1 M$	$5.953e * 10^{9}$	$5.767 * 10^{9}$	$6.854 * 10^{9}$	$6.502 * 10^{9}$	$6.051 * 10^{9}$
$\alpha_2 M$	$5.953e * 10^{9}$	$5.767 * 10^{9}$	$6.854 * 10^{9}$	$6.051 * 10^{9}$	$6.502 * 10^{9}$
$\frac{\eta}{k_1}$	$1 * 10^{12}$	$1.887 * 10^{9}$	$7.072 * 10^{6}$	$7.072 * 10^{6}$	$1.887 * 10^{9}$
$\frac{\eta}{k_2}$	$1 * 10^{12}$	$1.887 * 10^{9}$	$7.072 * 10^{6}$	$1.887 * 10^{9}$	$7.072 * 10^{6}$

Resulting averaged (with respect to realizations) attenuation estimations for P-wave (Fig. 15, left) and S-wave (Fig. 15, right) are demonstrated on for "stiff", "soft" and anisotropic fracture-filling materials. One can clearly see two peaks in "soft" material case, as well as in anisotropic material case for P-wave ans S-wave. Low frequency peak corresponds to FB-WIFF attenuation, and high-frequency peak corresponds to FF-WIFF attenuation mechanisms. High fracture connectivity through whole model results in high FF-WIFF peak attenuation in comparison with FB-WIFF peak for "soft" material case. "Stiff" material attenuation estimation for P-wave demonstrate only one peak, and that may be explained by

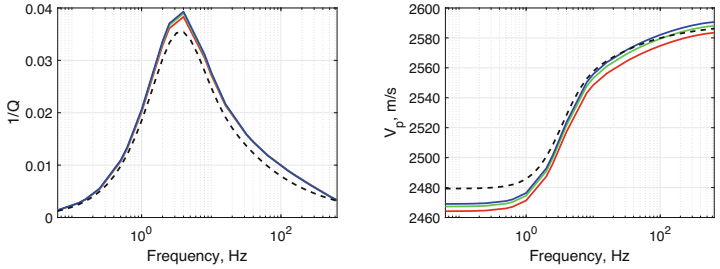

Fig. 11. Attenuation (left) and P-wave phase velocity (right) normal to layers. Colored curves represent numerical results (red for "square", green - "rectangular", blue - "thin" geometry). Black dashed lines represent analytical estimations from White's 1D model. (Color figure online)

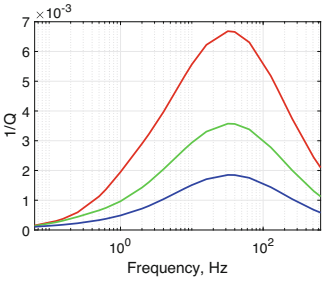

Fig. 12. Attenuation in direction along layers. Colored curves represent results for different domains: red for "square", green - "rectangular", blue - "thin" geometry. (Color figure online)

no significant fracture-to-fracture flow provided due to low permeability within the fractures. As the contrast between background and "stiff" fracture material permeabilities is still quite high, we still can note significant P-wave attenuation caused by FB-WIFF. Most interesting result is P-wave attenuation in anisotropic material case. Anisotropic case attenuation peak at low frequencies is flattened and lower than both other cases peaks, but in comparison with "stiff" material case, we can clearly observe the presence of the high frequency peak. This peak shows that in anisotropic case FF-WIFF is still significant, although it is much less than FF-WIFF peak in "soft" material case, as expected. For S-wave attenuation, we see much less attenuation at high frequencies for "stiff" case, and only low frequency FB-WIFF attenuation peak is clearly visible. FF-WIFF peak is also may be shifted in frequency is "stiff" material case, as we see relative small perturbation near 1 MHz. Indistinct of high frequency peak for S-wave attenuation in "soft" material case may be caused by the number of realizations with considered frequencies used in experiments.

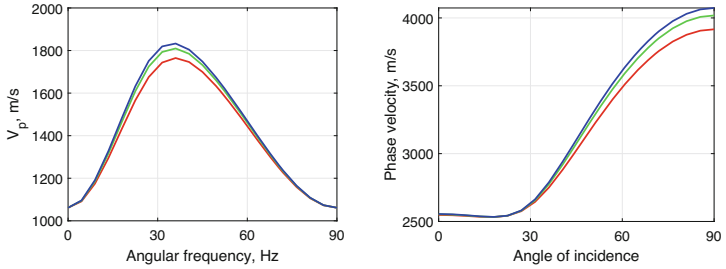

Fig. 13. P-wave (left) and S-wave (right) phase velocity as functions of incidence angle in horizontally layered media. The frequency 10 Hz. Colored curves represent results for different domains: red for "square", green - "rectangular", blue - "thin" geometry. (Color figure online)

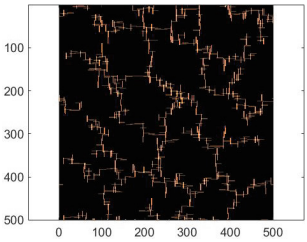

Fig. 14. Fractured media model. Black color represents background, yellow color represents fractures. (Color figure online)

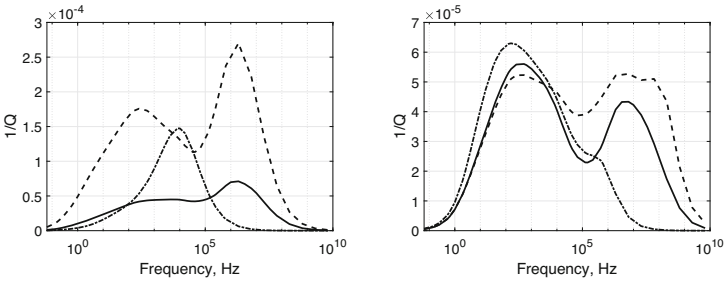

Fig. 15. P-wave (left) and S-wave (right) attenuation estimations for "stiff" (dash-dotted lines), "soft" (dashed lines) and anisotropic (solid lines) fracture-filling material.

6 Conclusion

Algorithm of numerical upscaling is presented to reconstruct effective viscoelastic stiffness tensor and estimate frequency-dependent attenuation in anisotropic fractured porous fluid-saturated media. Finite-difference approximation of quasi-static Biot equations is presented and applied to solve basic load test problems

and recover effective viscoelastic properties related to poroelastic fluid-saturated sample. Resulting effective viscoelastic stiffness tensor is used to estimate both seismic attenuation and phase velocity. Algorithm is applied to estimate seismic attenuation in highly connected fractured poroelastic media. Results show the effect of fracture-filling material properties and its microscale anisotropy on seismic attenuation caused by FB-WIFF and FF-WIFF. However, one of dominant attenuation mechanisms at high frequencies is scattering, so presented algorithm can be used combined with algorithms of attenuation estimation, which are able to take dynamic effects into account.

References

1. Bazaikin, Y., et al.: Effect of CT image size and resolution on the accuracy of rock property estimates. J. Geophys. Res. Solid Earth **122**(5), 3635–3647 (2017)
2. Biot, M.A.: Theory of propagation of elastic waves in a fluid-saturated porous solid. II. Higher frequency range. J. Acoust. Soc. Am. **28**, 179–191 (1956)
3. Biot, M.A.: Theory of propagation of elastic waves in fluid-saturated porous solid. I. Low-frequency range. J. Acoust. Soc. Am. **28**, 168–178 (1956)
4. Carcione, J.M., Cavallini, F.: A rheological model for anelastic anisotropic media with applications to seismic wave propagation. Geophys. J. Int. **119**, 338–348 (1994)
5. Carcione, J., Picotti, S.: P-wave seismic attenuation by slow-wave diffusion: effects of inhomogeneous rock properties. Geophysics **7**, O1–O8 (2006). https://doi.org/10.1190/1.2194512
6. Cheng, A.H.D.: Material coefficients of anisotropic poroelasticity. Int. J. Rock Mech. Min. Sci. **34**(2), 199–205 (1997)
7. Guo, J., Rubino, J.G., Glubokovskikh, S., Gurevich, B.: Effects of fracture intersections on seismic dispersion: theoretical predictions versus numerical simulations. Geophys. Prospect. **65**(5), 1264–1276 (2017)
8. Huang, F., et al.: The first post-injection seismic monitor survey at the Ketzin pilot CO_2 storage site: results from time-lapse analysis. Geophys. Prospect. **66**(1), 62–84 (2018)
9. Hunziker, J., et al.: Seismic attenuation and stiffness modulus dispersion in porous rocks containing stochastic fracture networks. J. Geophys. Res. Solid Earth **123**(1), 125–143 (2018)
10. Kong, L., Gurevich, B., Zhang, Y., Wang, Y.: Effect of fracture fill on frequency-dependent anisotropy of fractured porous rocks. Geophys. Prospect. **65**(6), 1649–1661 (2017)
11. Marty, N.C.M., Hamm, V., Castillo, C., Thiéry, D., Kervévan, C.: Modelling water-rock interactions due to long-term cooled-brine reinjection in the Dogger carbonate aquifer (Paris basin) based on in-situ geothermal well data. Geothermics **88**, 101899 (2020)
12. Masson, Y.J., Pride, S.R., Nihei, K.T.: Finite difference modeling of Biot's poroelastic equations at seismic frequencies. J. Geophy. Res. Solid Earth **111**(B10), 305 (2006)
13. Menke, H.P., Reynolds, C.A., Andrew, M.G., Pereira Nunes, J.P., Bijeljic, B., Blunt, M.J.: 4D multi-scale imaging of reactive flow in carbonates: assessing the impact of heterogeneity on dissolution regimes using streamlines at multiple length scales. Chem. Geol. **481**, 27–37 (2018)

14. Novikov, M.A., Lisitsa, V.V., Bazaikin, Y.V.: Wave propagation in fractured-porous media with different percolation length of fracture systems. Lobachevskii J. Math. **41**(8), 1533–1544 (2020). https://doi.org/10.1134/S1995080220080144
15. Ovaysi, S., Wheeler, M., Balhoff, M.: Quantifying the representative size in porous media. Transp. Porous Media **104**(2), 349–362 (2014)
16. Rubino, J.G., Muller, T.M., Guarracino, L., Milani, M., Holliger, K.: Seismoacoustic signatures of fracture connectivity. J. Geophys. Res. Solid Earth **119**(3), 2252–2271 (2014)
17. Rubino, J.G., Caspari, E., Müller, T.M., Milani, M., Barbosa, N.D., Holliger, K.: Numerical upscaling in 2-D heterogeneous poroelastic rocks: anisotropic attenuation and dispersion of seismic waves. J. Geophys. Res. Solid Earth **121**(9), 6698–6721 (2016)
18. Salaun, N., et al.: High-resolution 3D seismic imaging and refined velocity model building improve the image of a deep geothermal reservoir in the Upper Rhine Graben. Lead. Edge **39**(12), 857–863 (2020)
19. Solovyev, S., Novikov, M., Kopylova, A., Lisitsa, V.: Numerical solution of Biot equations in quasi-static state. In: Gervasi, O., et al. (eds.) ICCSA 2021. LNCS, vol. 12949, pp. 519–531. Springer, Cham (2021). https://doi.org/10.1007/978-3-030-86653-2_38
20. Vavrycuk, V.: Velocity, attenuation, and quality factor in anisotropic viscoelastic media: a perturbation approach. Geophysics **73**(5), D63–D73 (2008)
21. Xu, C., Dowd, P.A., Mardia, K.V., Fowell, R.J.: A connectivity index for discrete fracture networks. Math. Geol. **38**(5), 611–634 (2006)